Materials Today Bio 32 (2025) 101654

Contents lists available at ScienceDirect

Materials Today Bio

journal homepage: www.journals.elsevier.com/materials-today-bio

Enhancing clinical precision in lung cancer tissue biopsy through elevated response-threshold of an endoplasmic reticulum-targeted fluorogenic probe

Zhiyang Yuwen [a,b], Xinglong Chen [a], Kexin Chen [b], Tenglong Zou [b], Guojiang Mao [c], Hongwen Liu [b,*], Lemeng Zhang [a,**]

[a] Thoracic Medicine Department 1, The Affiliated Cancer Hospital of Xiangya School of Medicine, Central South University/Hunan Cancer Hospital, Changsha, 410013, PR China

[b] Key Laboratory of Chemical Biology and Traditional Chinese Medicine Research (Ministry of Education), College of Chemistry and Chemical Engineering, Hunan Normal University, Changsha, 410081, PR China

[c] Key Laboratory of Green Chemical Media and Reactions, Ministry of Education, School of Chemistry and Chemical Engineering, Henan Normal University, Xinxiang, 453007, PR China

ARTICLE INFO

Keywords:
Accurate diagnosis
High-response-threshold
ER targeting
Lung cancer biopsy
Fluorogenic probe

ABSTRACT

Lung carcinoma is the leading cause of mortality globally, posing a significant public health concern. Fluorescent-mediated tumor imaging is emerging as a novel diagnostic and therapeutic approach in clinical practice. Nevertheless, traditional probes lack accuracy in diagnosing tumors due to the overlap in baseline values of certain tumor biomarkers between normal and tumor cells as both exhibit turn-on fluorescence, rendering it impossible to distinguish tumor tissue from normal tissue with high resolution. We introduce a sensing strategy that constructs a probe with an elevated biomarker response-threshold and targeting ability for the endoplasmic reticulum (ER), enabling precise distinction between tumor and normal cells, and successfully develop such a probe. Elevating the response-threshold is advantageous in minimizing interference from baseline values of biomarkers in normal cells. Additionally, targeting the ER ensures that the probe's response range is consistent with the biomarker content in the ER, collectively enhancing differentiation between normal and cancer cells. Using this novel probe, a distinct bright fluorescence signal from tumors could be observed in confocal imaging of tumor tissues from tumor-bearing mice after intravenous injection, in stark contrast to the limited fluorescence emanating from normal tissues. Furthermore, this probe demonstrated exceptional precision in distinguishing clinical lung cancer tissue from para-cancer tissue. This work presents a more reliable tumor detection strategy, capable of accurate diagnosis even when the biomarker is highly expressed in both normal and tumor tissues. It promises to be a valuable tool for future clinical applications, particularly in intraoperative assisted resection.

1. Introduction

Among various malignant tumors, lung carcinoma exhibits the highest morbidity and mortality. The complete resection of the lesion site and the clearance of metastatic lymph nodes determine the prognosis of carcinoma patients [1,2]. Accurate diagnosis of lung cancer constitutes an essential prerequisite for cancer treatment [3,4]. The crux and challenge of cancer diagnosis reside in the discrimination of cancerous cells/tissues from normal ones. Lung cancer progress slowly in the early phases and fail to develop a typical pathological morphologic structure. Nevertheless, alterations have actually occurred within the cells/tissues, which differ from normal cells/tissues. Relying solely on morphology is prone to misdiagnosis of inflammation or other disorders [5]. Hence, the development of techniques capable of precisely differentiating between cancer cells and normal cells, thereby indicating the boundary between cancerous and normal tissues, is of great value for the accurate diagnosis of lung cancer and subsequent symptomatic treatment [4,6]. In addition, the recurrence of the tumor mainly results from incomplete clinical surgical resection. Specifically, given the absence of effective approaches to clearly delineate the boundary between normal tissue and tumor tissue, it is challenging for surgeons to detect and precisely remove metastatic tumors based on visual

* Corresponding author.
** Corresponding author.
E-mail addresses: liuhongwen@hnu.edu.cn (H. Liu), zhanglemeng@hnca.org.cn (L. Zhang).

https://doi.org/10.1016/j.mtbio.2025.101654
Received 19 January 2025; Received in revised form 19 February 2025; Accepted 9 March 2025
Available online 10 March 2025

inspection and palpation. Hence, it is of urgent necessity to develop a highly discriminatory detection method for tumor and normal tissue to assist in clinical diagnosis and treatment.

Fluorescence detection has emerged as a powerful tool for monitoring a wide array of physiological and pathological processes in real-time, at both the cellular and molecular levels. This technique holds considerable promise for tumor screening, as evidenced by numerous studies conducted over the past decades [7–15]. Various tumor biomarker-activated fluorescent probes have been developed for imaging and detecting cancer. These probes primarily rely on the differences in endogenous substance content or microenvironmental characteristics between tumor and normal tissues, encompassing enzymes, biothiols, reactive oxygen species (ROS), reactive nitrogen species (RNS), pH levels, viscosity, and other factors [16–23]. However, few probes can effectuate effective differentiation. This limitation stems from the high sensitivity of these probes, which often leads to an inability to distinguish between cancer tissue and normal tissue due to their susceptibility to interference from normal tissues [5,8,24]. The primary reason for this phenomenon lies in the fact that certain biomarkers are present a certain baseline value in normal cells, thereby leading to the highly sensitive probe demonstrating intense fluorescence in both tumor and normal cells [20]. To address this issue, previous works have proposed dual-locked systems to enhance the precision in cancer identification [25]. While this strategy has proven effective in improving diagnostic accuracy, it may result in false negative signals due to the two-step reaction activation process, which inherently compromises sensitivity. Therefore, we introduce a novel approach aimed at increasing the response threshold of biomarker-activable fluorescence probe to enhance precision in clinical lung cancer tissue biopsy. Our approach involves two key innovations to avoid interference from the baseline values of normal intracellular biomarkers. Firstly, we elevate the probe's response threshold towards the biomarker by leveraging the steric hindrance effect in the reaction. Secondly, recognizing the uneven distribution of some biomarkers within the cytoplasm and organelles, we further enhance reliable differentiation through the specific organelle targeting capability of the probe. To tackle the aforementioned challenge comprehensively, we have integrated this strategy and designed a high-threshold organelle-targeting fluorescent probe that achieves reliable discrimination between normal cells and cancer cells for enhanced precision in clinical lung cancer tissue biopsy.

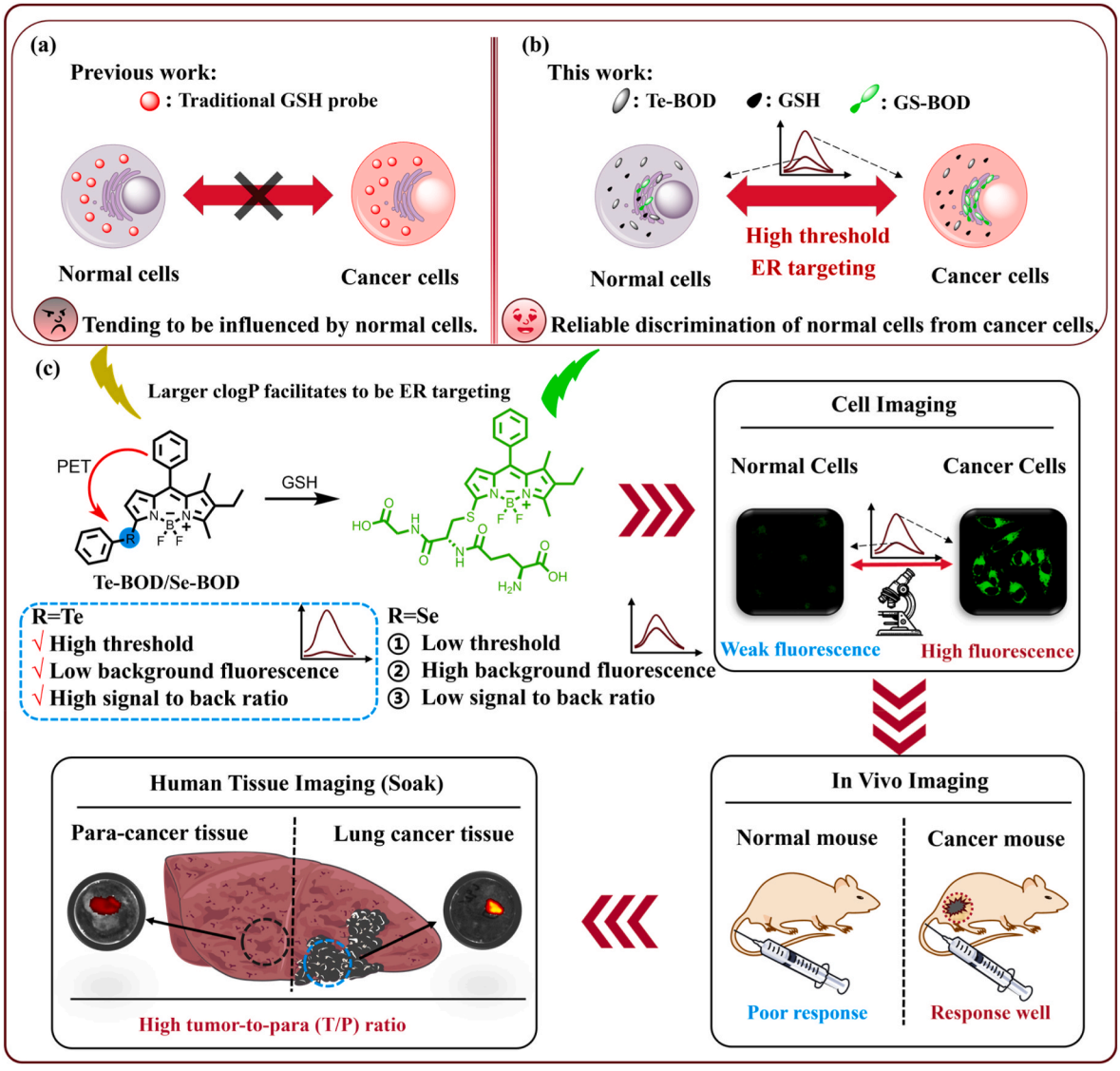

Scheme. 1. Design strategy for high threshold response fluorescent probe and reliable discrimination between normal and tumor cells/tissues. (a). Previous GSH fluorescent probes are not appropriate for differentiating normal cells from cancer cells because of their high sensitivity. (b). A novel GSH sensing strategy used for the reliable discrimination of normal cells from cancer cells. (c) The response mechanism of this probe and the reliable discrimination of tumor tissue, para-cancer tissue, and normal tissue by high response-threshold.

Among various biomarkers, glutathione (GSH), an important biothiol, is widely used as the cancer biomarker to design activable probe. However, GSH is present in high levels in both normal and tumor cells with concentration of 1–5 mM for normal cells and higher concentration (about 5–20 mM) for cancer cells, respectively [26,27]. Despite the numerous reports on GSH probes [28–31], they are highly sensitive (Table S1), and low concentrations of GSH (significantly below baseline levels) will saturate the fluorescence response, which is detrimental to the discrimination between normal tissues and tumors (Scheme 1a). Chan et al. developed a GSH-insensitive probe for lung cancer diagnosis via photoacoustic imaging [32]. Although the detection effect is notable, the hemicyanine probe might be influenced by the high concentration of ROS in tumors, leading to inaccurate detection outcomes [33]. It has been reported that the distribution of GSH in organelles is uneven, namely, 10–15 % in mitochondria and approximately 5 % in the endoplasmic reticulum (ER) and nucleolus [34]. The selection of ER targeting is further conducive to the discrimination between normal cells and cancer cells. Although a few examples of ER-targeted GSH probes have been reported [35–37], they merely investigated the alterations in GSH content under diverse physiological conditions of cells and were not employed to discriminate normal cells from cancer cells, owing to the high sensitivity of these probes, and even 5 % of the GSH content of normal cells is sufficient to saturate the probe response, which significantly limits the accuracy of their detection. Consequently, it remains indispensable to develop a high-threshold ER-targeted GSH fluorescent probe through rational design for reliably discriminating normal cells from cancer cells.

In this study, we rationally designed an ER-targeted GSH fluorescent probe with a high response threshold, specifically for enhancing clinical precision in lung cancer tissue biopsy (Scheme 1). The probe possesses high lipid solubility to rapid targeting of the ER. Meanwhile, the probe has an extremely high response threshold to GSH, 100 μM GSH can merely induce weak fluorescence enhancement of the probe. Our objective is to discover a suitable approach to increase the threshold of probe response with GSH. In our previous research, we developed a novel fluorescence probe for GSH detection by means of the assembly and de-assembly strategy based on a specific GSH recognition site, phenyl-selenium (PSE) group [38]. However, the *J*-aggregation is unstable in vivo, thereby resulting in the enhancement of the background fluorescence of the probe. Hence, we aim to replace PSE with phenyl-tellurium (PTE) on this basis as we propose that Te atoms possess a larger atomic radius and the greater steric hindrance might attenuate the nucleophilic addition ability of GSH. The fluorescence response experiment indicated that the PTE group significantly raised the threshold of the probe's response to GSH, and the PSE modified probe was utilized as the control. Owing to the high threshold of the probe to GSH, we were able to achieve a reliable distinction between normal and tumor cells. Most importantly, we have successfully discriminated clinic lung cancer tissue from adjacent tissue based on the fluorescence intensity of the probe. For treatment, fluorescence probe can assist in identifying the risk of the tumor edge and distant metastasis, thereby guiding precise tumor resection, reducing the risk of tumor recurrence and metastasis, protecting the patient's healthy lung tissue, and further prolonging the patient's life.

2. Experimental section

2.1. Experimental procedures

Unless otherwise specified, absorption and fluorescence spectra were measured in 10 mM PBS buffer (pH 7.4, containing 50 % DMSO) at 37 °C. A stock solution of **Te-BOD** (1 mM) was prepared in DMSO, and a working solution was obtained by mixing 10 μL of the stock solution with 500 μL of PBS buffer and 490 μL of DMSO to achieve a final concentration of **Te-BOD** at 10 μM. For fluorescence experiments, an appropriate amount of analyte solution was added to the probe solution to prepare the test samples. The UV–Vis spectrum was recorded over the range of 400–700 nm, and the fluorescence spectrum was measured from 520 to 650 nm with an excitation wavelength of 480 nm (slit widths, 5 nm/5 nm).

2.2. Cell culture and cytotoxicity assay

L929, HUVEC, 293T, H1299, A549, MCF-7, Luc-4T1, HepG2, and Hep3B cells were cultured in Gibco's DMEM medium supplemented with 10 % fetal bovine serum (FBS) and 1 % penicillin/streptomycin (dual antibiotics), and maintained in a humidified incubator with 5 % CO_2 at 37 °C.

2.3. Cytotoxicity assay

Initially, 4T1, A549, and HUVEC cells were seeded into 96-well plates following a 6 × 6 layout. After cell culture, the probe **Te-BOD** at various concentrations (0, 2, 4, 6, 8, 10 μM) was added to the plates, and cytotoxicity was assessed using the MTT colorimetric assay. The absorbance at 490 nm was measured by using a microplate reader. Cell viability was determined using the following formula: Cell viability ratio (%) = $(OD_{Sample} - OD_{PBS})/(OD_{Blank} - OD_{PBS}) \times 100$ %.

2.4. In vivo imaging

A subcutaneous tumor model was established through subcutaneous injection of LA-795 cells in mice. **Te-BOD** (20 μL, 200 μM) was respectively injected into normal tissue and the tumor site for fluorescence imaging. In the inhibition group, 30 μL of 5 mM NEM was injected into the tumor site and the normal tissue site for 30 min, followed by injection of the probe for imaging. Intravenous injection was carried out by injecting a 20 μL 200 μM probe via the tail vein, followed by fluorescence imaging. All live cells and live animal operations were in accord with institutional animal use and care regulations, according to protocol No. SYXK (Xiang) 2020-0012, approved by Laboratory Animal Center of Hunan.

2.5. Clinical lung cancer tissue imaging

Clinical lung cancer and para-cancer tissues were obtained from Hunan Cancer Hospital. The samples consisted of surgically removed lung tumors and a certain extent of surrounding tissues (para-cancer tissues). The samples were resected and stored at 0 °C. Fluorescence imaging was performed on tumor tissues from patients clinically diagnosed with lung cancer within 3 h post-sample collection. Larger tumor samples (approximately 0.5 × 1.5 × 0.2 cm), along with para-cancer tissues harvested from the operating table, were placed in a sterile dish. The tissue is immersed in a solution of the probe (200 μM, 1 mL) and then imaged. All the clinical experiments were approved by the Medical Ethics Committee of Hunan Cancer Hospital (No. 135).

3. Results and discussion

3.1. Design and synthesis of the Te-BOD

Given that tumor cells/tissues encompass a high concentration of oxidizing substances, to guarantee the reliability of fluorescence detection, we selected BODIPY as a dye molecule due to its excellent chemical stability and light stability [33,39]. Since both normal and cancer cells possess high concentrations of GSH, it is of critical importance to elevate the threshold of the probe's response to GSH for achieving the discrimination between normal and cancer cells. We hypothesize that Te atoms have larger atomic radii compared to Se atoms, which might enhance the steric hindrance of GSH during nucleophilic substitution, thereby reducing the threshold of response (Fig. S1). Therefore, we replace the Cl atom on BODIPY with PTE to obtaining **Te-BOD**, and

employ **Se-BOD** as a control. In addition, ER targeting constitutes another crucial factor for further attaining reliable discrimination between normal and cancer cells. Given that only approximately 5 % of total GSH is present in the ER [34], and this GSH content might be within the response range of the probe, thereby ensuring the accuracy of the detection. ER is a good lipid-soluble system. Probes with high lipid solubility typically possess a hydrophobic structure and can be embedded within the lipid bilayer [40–42]. This characteristic enables them to bind to the ER more readily rather than remaining in the cytoplasm or other hydrophilic regions. The lipophilicity of fluorescent molecules can be evaluated through a calculated clogP. It has been reported that specific targeting to the ER demands appropriate lipophilicity (clogP >3.4) [43], and the clogP of **Te-BOD** is approximately 8.69. Thus, the probe is expected to possess a strong ability for ER targeting. After the probe was designed and synthesized, the properties of the probe were investigated.

3.2. Spectral properties of Te-BOD

Firstly, the influence of different organic concentrations on the solubility of the probe was investigated by UV spectroscopy. As depicted in Fig. 1a and Fig. S1a, both **Se-BOD** and **Te-BOD** present obvious H/*J*-aggregation absorption peaks when the organic term concentrations are below 50 %. No aggregation peak was observed in 50 % and 70 % organic terms. Our objective was to design fluorescent probes targeting the endoplasmic reticulum, which possesses higher lipophilic than other organelles on account of its involvement in lipid metabolism and protein folding [44]. The ER membrane, consists of 50 % phospholipids and 20 % protein [45]. Hence, we selected 50 % organic phases to simulate the microenvironment of the ER and then we investigated the fluorescence

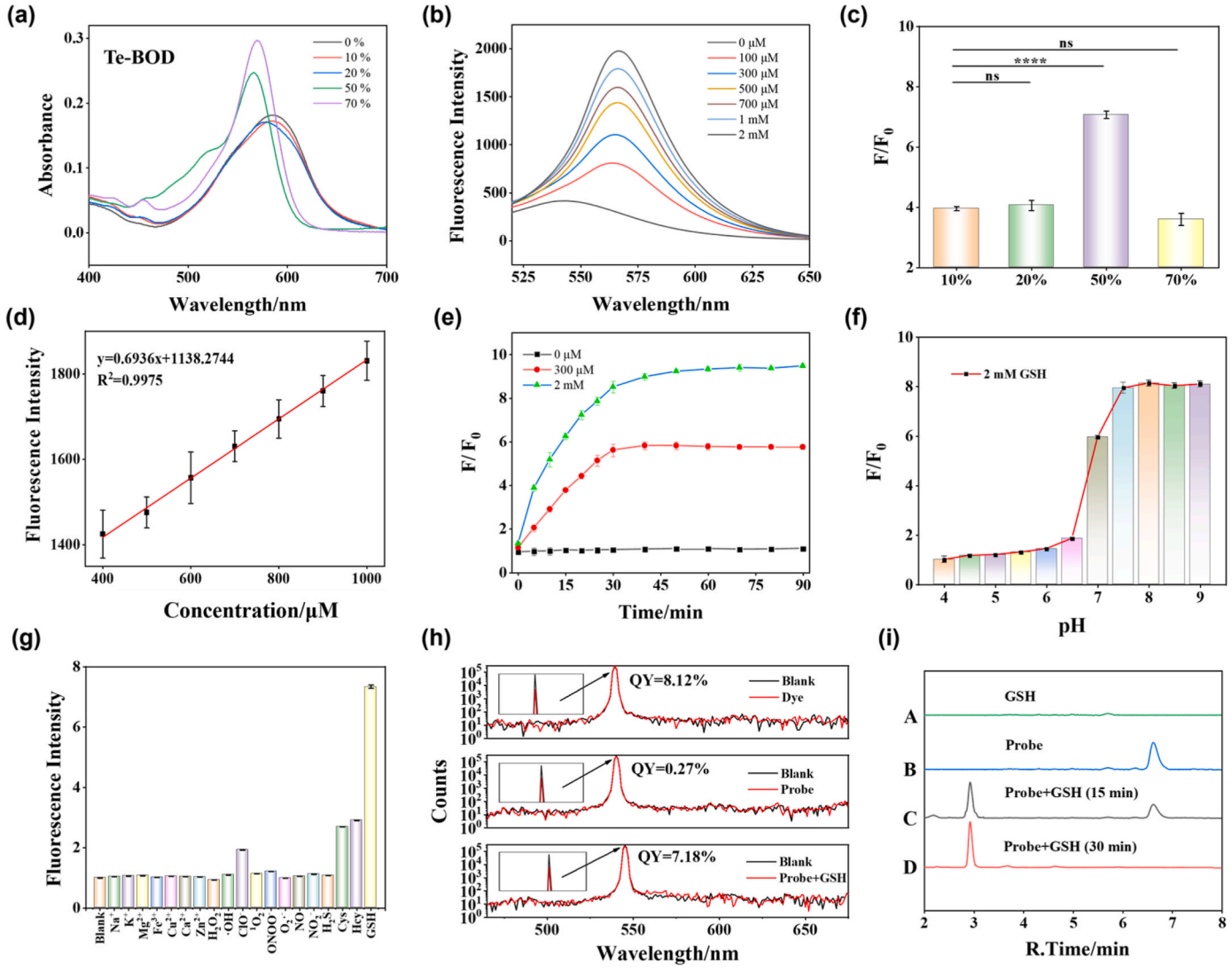

Fig. 1. Fluorescence response of **Te-BOD** (10 μM) to GSH and mechanism verification. (a). Absorption spectra of **Te-BOD** in different proportion DMSO. (b). Fluorescence response of **Te-BOD** to difference concentration of GSH in PBS containing 50 % DMSO. (c). The fluorescence response ratio of Te-BOD to 2 mM GSH in different proportion organic phases. (*P < 0.1, **P < 0.01, ***P < 0.001, ****P < 0.0001). (d). Relationship corresponding to the activatable fluorescence intensity at 565 nm versus 400–1000 μM GSH. (e). Time-dependent fluorescence enhancement ratio of **Te-BOD** to difference concentration of GSH in PBS containing 50 % DMSO. (f). pH effect of the fluorescence response of **Te-BOD** at 565 nm in the presence of 2 mM GSH. (g). Fluorescence changes of **Te-BOD** in the presence of various biomolecules. Na^+ (100 μM), K^+ (100 μM), Mg^{2+} (100 μM), Fe^{3+} (100 μM), Cu^{2+} (100 μM), Ca^{2+} (100 μM), Zn^{2+} (100 μM), H_2O_2 (40 μM), ·OH (40 μM), ClO^- (40 μM), $^1O_2$ (40 μM), $O_2^{\cdot-}$ (40 μM), $ONOO^-$ (40 μM), NO (100 μM), NO_2^- (100 μM), H_2S (100 μM), Cys (100 μM), Hcy (100 μM), GSH (2 mM), pH 7.4. 10 mM PBS containing 50 % DMSO. (h). Absolute fluorescence quantum yields of Cl-BOD (Dye), **Te-BOD** (Probe) and Probe + GSH; Dye: λ_{ex} = 545 nm. Probe: λ_{ex} = 545 nm. Probe + GSH: λ_{ex} = 548 nm. (i). HPLC traces of probe with GSH to propose the sensing mechanism of **Te-BOD** toward GSH. λ_{ex} = 480 nm, λ_{em} = 565 nm. Values are mean ± s.d. (n = 3).

response of two probes to GSH (Fig. 1b, Fig. S1b and Fig. S2). The background fluorescence of **Se-BOD** is significantly higher than that of **Te-BOD** at the same conditions, endowing the larger signal-to-back (S/B) ratio of **Te-BOD** than that of **Se-BOD**. The fluorescence response of both probes reaches saturation in the presence of 2 mM GSH, with 2.0 and 7.5-fold fluorescent enhancement respectively. In conclusion, it is determined that **Te-BOD** has a superior S/B ratio compared to **Se-BOD**. With the further increase of GSH concentration, the fluorescence intensity of the probe declined (Figs. S3a and 3b). In addition, the absorption spectrum of the **Te-BOD** undergoes a significant decrease upon the addition of 5 mM GSH and the color turns light yellow (Fig. S3c), suggesting that the conjugate structure might be disrupted. This might be attributed to the nucleophilic addition of a high concentration of GSH (>3 mM) to BODIPY (Fig. S3d) [46,47]. This result may cause the probe to exhibit weak fluorescence in other organelles or cytoplasm with a high GSH content within the cell, except for the ER, and to show strong fluorescence only in the ER. In addition, **Te-BOD** merely exhibited a favorable response under the most similar conditions of the ER microenvironment, and failed to demonstrate a good response in other circumstances (Fig. 1c–and Fig. S4, S5). This also facilitated the probe to generate a distinct fluorescence enhancement exclusively in the ER upon entering the cell. Subsequently, we elaborately investigated the fluorescence response of GSH to **Te-BOD** and verified the reaction mechanism under 50 % organic phase conditions. As depicted in Fig. 1d, the probe manifested a favorable linear fluorescence enhancement within the GSH concentration range of 400 μM–1000 μM. Based on the actual minimum response concentration of the probe towards GSH (>100 μM), the limit of detection (LOD) of the probe for GSH is 40 μM, which is conspicuously higher than that of the traditional GSH probe (typically less than 1 μM) [28]. By enhancing the steric hindrance effect of Te atoms with larger atomic radius, we managed to increase the threshold of the probe's response to GSH, which is nearly a hundred times higher than that of the reported GSH fluorescent probes' threshold, and thus is more suitable for reliable discrimination between normal and cancer cells. More significantly, the detection range of **Te-BOD** might lie within the GSH content range of the ER, thereby facilitating reliable imaging. Additionally, the higher threshold will possess greater accuracy in discriminating between normal and cancer cells compared with traditional highly sensitive ER target GSH probes [48]. The probe could react with GSH effectively within 60 min (Fig. 1e) and exhibited optimal fluorescence response at physiological pH (Fig. 1f). We further investigated the fluorescence behavior of the **Te-BOD** toward GSH and various biological species containing thiol, ROS, anions, and cations (Fig. 1g). The results demonstrated that the probe exhibited high specificity to GSH, while no significant signal fluctuation was observed in the presence of other analytes. The absolute fluorescence quantum yields of **Te-BOD** (probe) and Cl-BOD (dye) were measured, and it was demonstrated that PTE group effectively quenched the fluorescence of Cl-BOD (Fig. 1h). The absolute fluorescence quantum yield increases after the probe reacts with GSH, which is consistent with our fluorescence spectral response results. The absolute fluorescence quantum yield of **Se-BOD** (Fig. S1d) is higher than that of **Te-BOD**, suggesting that the PET effect of the PTE group is superior to that of the PSE. We employed high performance liquid chromatography (HPLC) to further validate the reaction mechanism of **Te-BOD** and GSH (Fig. 1i). The results were in accordance with the anticipated mechanism, with PTE serving as the recognition moiety for sulfhydryl nucleophilic substitution and the fluorescence quenching group being eliminated upon reaction with GSH, thereby restoring the fluorescence. We further verified the reaction mechanism through mass spectrometry (Fig. S6). To guarantee the accuracy of the probe monitoring results, we also explored the stability of the probe **Te-BOD** against ROS which are usually present in high concentrations in tumor cells. As depicted in Fig. S7a, the absorption spectrum of the probe did not change significantly even in the presence of a relatively high concentration of ROS. It has been reported that ClO^- oxidizes Te atoms and gives rise to fluorescence turn-on, which can be recovered in the presence of GSH [49]. As depicted in Figs. S7c, 30 μM ClO^- can result in a weak fluorescence enhancement of probe, while ClO^- concentrations below 30 μM showed almost no significant fluorescence response (Fig. S7d). ClO^- is primarily generated by the myeloperoxidase (MPO) system in neutrophils and macrophages. These cells produce ClO^- during immune responses to kill pathogens. In non-immune cells, the content of ClO^- is typically low. Some literature reports that the intracellular concentration of ClO^- may be around 30 μM [50]. The ER hardly contains MPO, and under normal conditions without external stimulation, it does not produce ClO^-. The time response of the probe to ClO^- indicates that its reaction with ClO^- is very slow, taking about 60 min to reach saturation (Fig. S7e). However, our probe can rapidly target the ER (in less than 5 min, Fig. 2c). Within such a short time frame, the ClO^- in the cells does not significantly affect the probe. After targeting the ER, the probe mainly reacts with GSH, so ClO^- does not interfere with the probe's detection performance. In addition, when subjected to continuous laser irradiation for 30 min, the probe demonstrated outstanding optical stability both in the absence and presence of GSH (Fig. S8). The above experiments suggest that **Te-BOD** has the potential to reliably differentiate between normal cells and cancer cells.

3.3. *Imaging of living cells with Te-BOD*

Owing to the excellent sensing performance of the probe, we endeavored to employ the probe for the reliable discrimination between normal cells and cancer cells. Prior to conducting live cell imaging, the cytotoxicity experiment of **Te-BOD** was carried out by MTT assay. Under the condition where the probe concentration reached up to 10 μM and the incubation time was 24 h, 4T1, A549 and HUVEC cells still maintained high viability, which clearly demonstrated the negligible cytotoxicity of the probe (Fig. S9). In the design of the probe, it is our aspiration to achieve that the probe can rapidly target ER and subsequently respond to the GSH within ER (Fig. 2a). Firstly, we verify the mechanism of the probe's response in the cells. We selected A549 cells and HUVEC cells for co-localization experiments, and the experimental outcomes indicated that the probe was predominantly located in ER (Fig. 2b, Fig. S10 and Fig. S11) due to its larger clogP than the requirement of ER targeting (clogP >3.4), it has a tendency to target ER. The time response experiments of the probe within the cell demonstrated that the fluorescence of the probe was gradually intensified in the portion overlapping with the ER tracker, which verified that the probe could rapidly target ER after entering the cell and generate fluorescence mainly through reacting with the GSH in the ER (Fig. 2c, Fig. S12 and Fig. S13). It has been reported that the pH value of the ER is approximately 7.20 [51], and the probe demonstrates the optimal fluorescence response to GSH around pH 7.2 (Fig. 1f). Thus, pH does not exert an influence on the fluorescence response of the probe. It is generally held that GSH in ER is more oxidizing than that in other non-secretory organelles such as mitochondria, the nucleus, or cytoplasmic plasma because ER is where disulfide bonds are synthesized and transferred to nascent secreted proteins and membrane proteins, and the formation of disulfide bonds is a key process for protein synthesis in ER [52]. The highly oxidative environment is necessary for the ER to fulfill its function, during which the majority of GSH is oxidized to GSSG [53]. Our probe rapidly targets ER and subsequently reacts with GSH in ER. Furthermore, we carried out long-term fluorescence imaging, and the experimental outcomes demonstrated that the probe was capable of imaging the ER with high contrast over an extended period of time (Fig. 2d and e). Even at 240 min, there were still signals and favorable localization coefficients. This might be attributed to the prolonged retention of the probe in ER and the destruction of the diffused probe by the high concentration of GSH in the cytoplasm. Therefore, the detection threshold and upper limit of GSH detection of our probe may be applicable to the precise differentiation between normal cells and cancer cells.

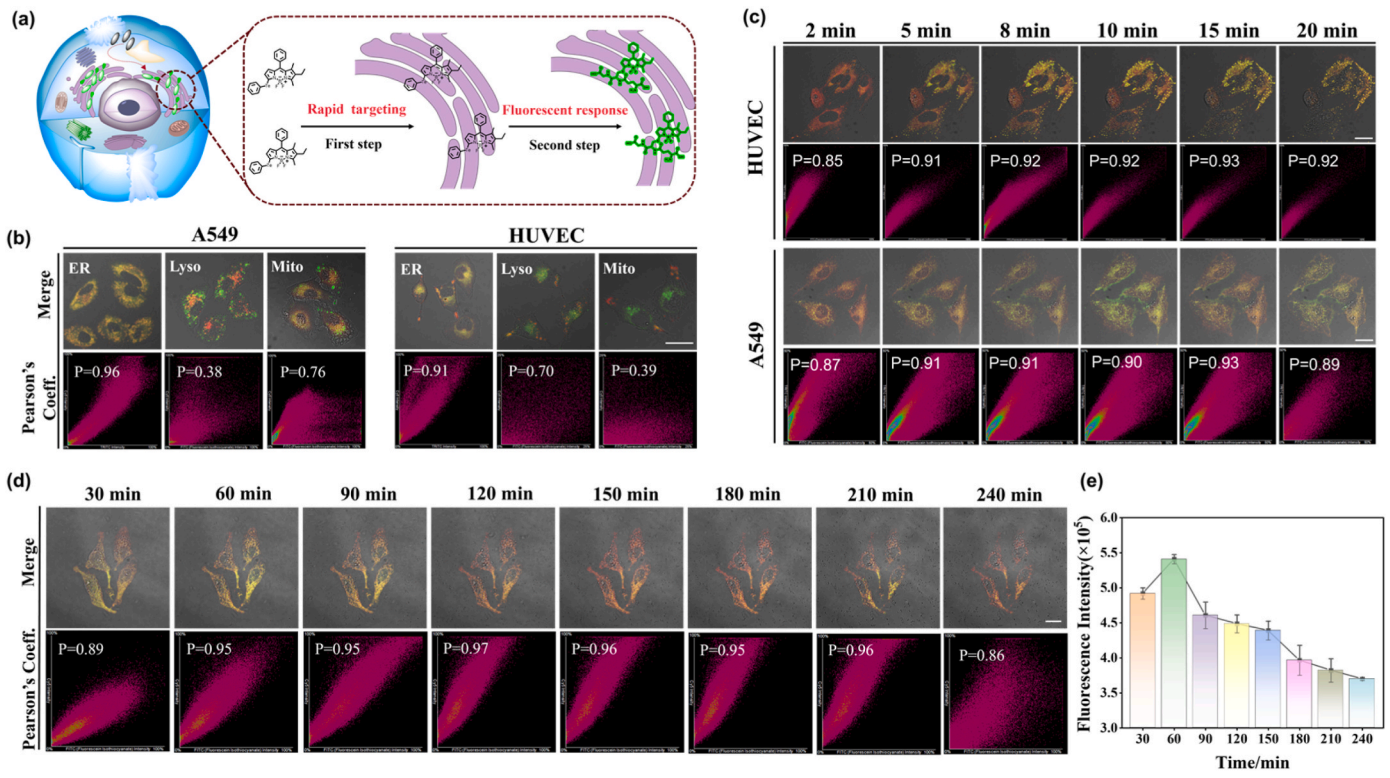

Fig. 2. Verification of the cell imaging mechanism. (a) Possible mechanism of probe in cell imaging. (b) A549 and HUVEC cells were incubated with **Te-BOD** (10 μM) and the co-locating reagents (ER: ER-Tracker Red, Lyso: Lyso-Tracker Red, Mito: Mito-Tracker Red. (c) Real time co-localization imaging was performed on HUVEC and A549 cells after staining with ER-Tracker Red and subsequent treatment with **Te-BOD** (10 μM). (d) Long-term co-localization imaging was performed on A549 cells after staining with ER-Tracker Red and subsequent treatment with **Te-BOD** (10 μM). The green channel was set to detect fluorescence within the range of 510–570 nm, excited at 488 nm. The red channel was configured to detect fluorescence within the range of 570–640 nm, excited at 561 nm. Scale bar: 25 μm.

The response mechanism of the probe within the cell was in line with our anticipated design, and subsequently, we employed the probe for fluorescence imaging of both normal and cancer cells. Three normal cells (L929, HUVEC, and 293T) and six cancer cells (Hep3B, MCF-7, H1299, Luc-4T1, A549, and HepG2) were selected for cell imaging (Fig. 3a). Because the ER of normal cells contains a lower level of GSH compared to that of cancer cells, merely extremely weak fluorescence could be observed in them. The cancer cells led to significant fluorescence, which was approximately 8–9 times enhanced in all cancer cells in comparison with HUVEC cells (Fig. 3c). To validate the responsiveness of the probe to intracellular GSH, we employed NEM, a thiol depleting agent, to manifest that the probe selectively reacts to GSH. NEM was initially incubated with the above normal cells and cancer cells for 30 min, followed by the addition of the probe (Figs. S14 and S15). It was noted that the fluorescence of both normal cells and cancer cells was lower than that of the group without NEM, suggesting that the probe truly selectively responded to GSH in ER. In contrast, normal cells (HUVEC) and cancer cells (Hep3B) were incubated with **Se-BOD** for fluorescence imaging (Fig. S16). The experimental results indicated that the fluorescence intensity in cancer cells was less than 2-fold higher than that in normal cells due to the low S/B ratio of the **Se-BOD**, and the contrast was poor, thereby making it challenging to distinguish normal cells from cancer cells. Subsequently, flow cytometry was employed to further validate whether the probe could precisely discriminate between normal cells and cancer cells. As depicted in Fig. 3d, in contrast to HUVEC cells, A549 cells manifested stronger fluorescence, and the fluorescence intensity was significantly decreased upon the addition of inhibitors, which was in accordance with our confocal imaging outcomes.

To further validate that our probe can effectively discriminate normal cells from cancer cells, normal cells (HUVEC) and cancer cells (Hep3B) with distinct morphological disparities were co-cultured and confocal imaging was conducted (Fig. 3e). HUVEC cells presented an irregular morphology being slightly larger and presenting a darker coloration, whereas Hep3B cells were pebble-shaped. These two cell lines were selected to facilitate the identification by our eyes. After the addition of the probe, Hep3B cells manifested brighter fluorescence than HUVEC cells, indicating that the probe was capable of distinguishing normal cells from cancer cells even in the immediate state of cell mixture. The aforementioned conclusions substantiate that **Te-BOD** holds the potential to reliably distinguish between normal cells and cancer cells. There exist several approaches for the detection of clinical lung cancer, such as imaging, blood tests, and pathology. Among these, pathological examination serves as the gold standard for clinical diagnosis. The principal method involves extracting sputum or pleural puncture liquid specimens and identifying whether the cells are cancerous under the microscope through the naked eye. This approach is relatively challenging since the cells in body fluids are complex and have diverse shapes, which may lead to erroneous detection. We attempted to apply the probe for fluorescence imaging of pleural effusion in clinical patients with lung disease. Under the microscope, we observed significant variability in pleural effusion among different patients. In mild cases, the pleural effusion was relatively clear with few cells, while in severe cases, it appeared slightly turbid and contained various types of cells. We selected pleural effusion from relatively severe patients for fluorescence imaging because their cells are more complex and present greater challenges. As shown in Fig. S17, we observed that among the numerous cells, most exhibited weak fluorescence, while a few cells displayed strong fluorescence (Red circle). We speculate that these may be cancerous cells. Moreover, cancer cells typically exhibit cluster distribution, which is consistent with our experimental results. If this clinical sample were analyzed solely based on cell morphology (clinical

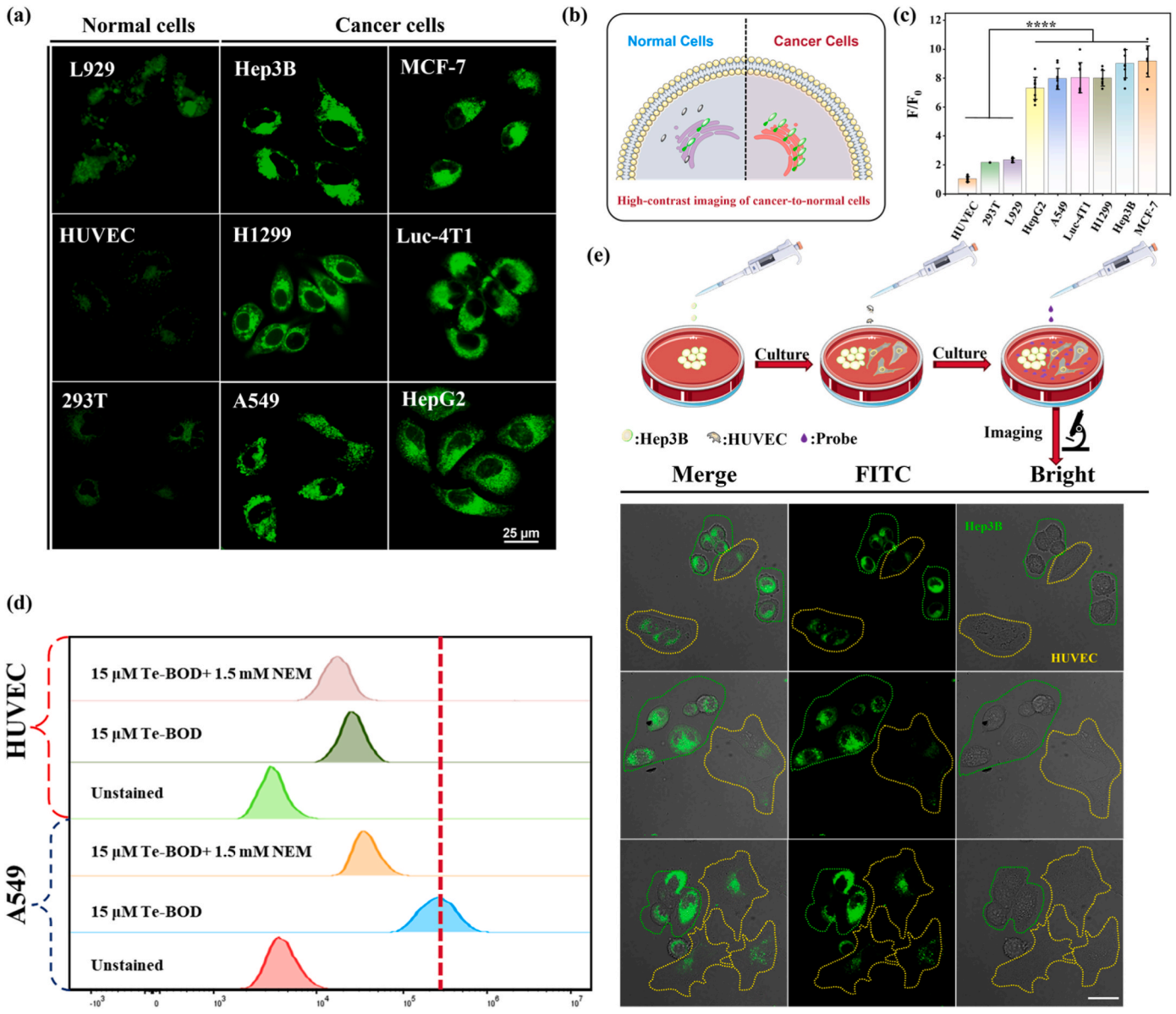

Fig. 3. Imaging and discrimination between normal and cancer cells. (a) Fluorescence imaging of various cell lines following incubation with **Te-BOD** (10 μM). (b) A diagram of **Te-BOD** for discriminating between normal and cancer cells. (c) Relative fluorescence intensity in (a). (d) Flow cytometry experiment. (e) Fluorescence imaging of mixed culture cells treated with **Te-BOD**. Hep3B (green region) and HUVEC (yellow region). $\lambda_{ex} = 490$ nm, $\lambda_{em} = 510–550$ nm. Scale bar: 25 μm *P < 0.1, **P < 0.01, ***P < 0.001, ****P < 0.0001.

cytological examination), it might lead to misdiagnosis due to the large number of cells present. Our fluorescent probe demonstrates outstanding performance in differentiating between normal and cancer cells and can distinguish the cells by fluorescence intensity with higher accuracy and speed compared to the clinical gold standard.

3.4. Imaging of tumor bearing mice by Te-BOD

Encouraged by the outstanding performance of **Te-BOD** at the cellular level, the capacity of **Te-BOD** to discriminate tumors from normal tissues in mice was evaluated. First, we investigated the time-dependent imaging of endogenous GSH in normal tissue and tumor-bearing tissue by the probe. As shown in Fig. 4a, fluorescence in the tumor gradually enhanced with time and reached a plateau at about 70 min. Due to the high-threshold of probe and the emission wavelength of the probe was short and the penetration depth was limited, there was almost no obvious fluorescence change in normal tissue. At 70 min, the fluorescence of tumor site was enhanced nearly 4 folds, which was significantly different from normal tissue (Fig. 4b). We subsequently utilized other tumor-bearing mice to conduct fluorescence imaging at 70 min after the injection of the probe (Fig. 4c). The experimental outcomes indicated that the probe exhibited obvious fluorescence enhancement at the tumor sites, but almost no fluorescence enhancement at the normal tissue sites. To prove that the probe responds to GSH in the tumor, we injected NEM into the tumor for 30 min and then injected the probe for imaging. The fluorescence intensity of the tumor site was significantly reduced, and the fluorescence intensity was similar to that of the normal tissue where the probe was injected. Compared with normal tissues (Fig. 4d), the fluorescence enhancement at the tumor sites was 3–4 folds, while the fluorescence of the tumor sites with NEM was significantly weakened, showing only 1.5 times of fluorescence enhancement. Subsequently, confocal tissue imaging of the injected probe tumors, the NEM-pretreated tumors, and normal tissues excisions was conducted (Fig. 4e). The tissue imaging revealed that

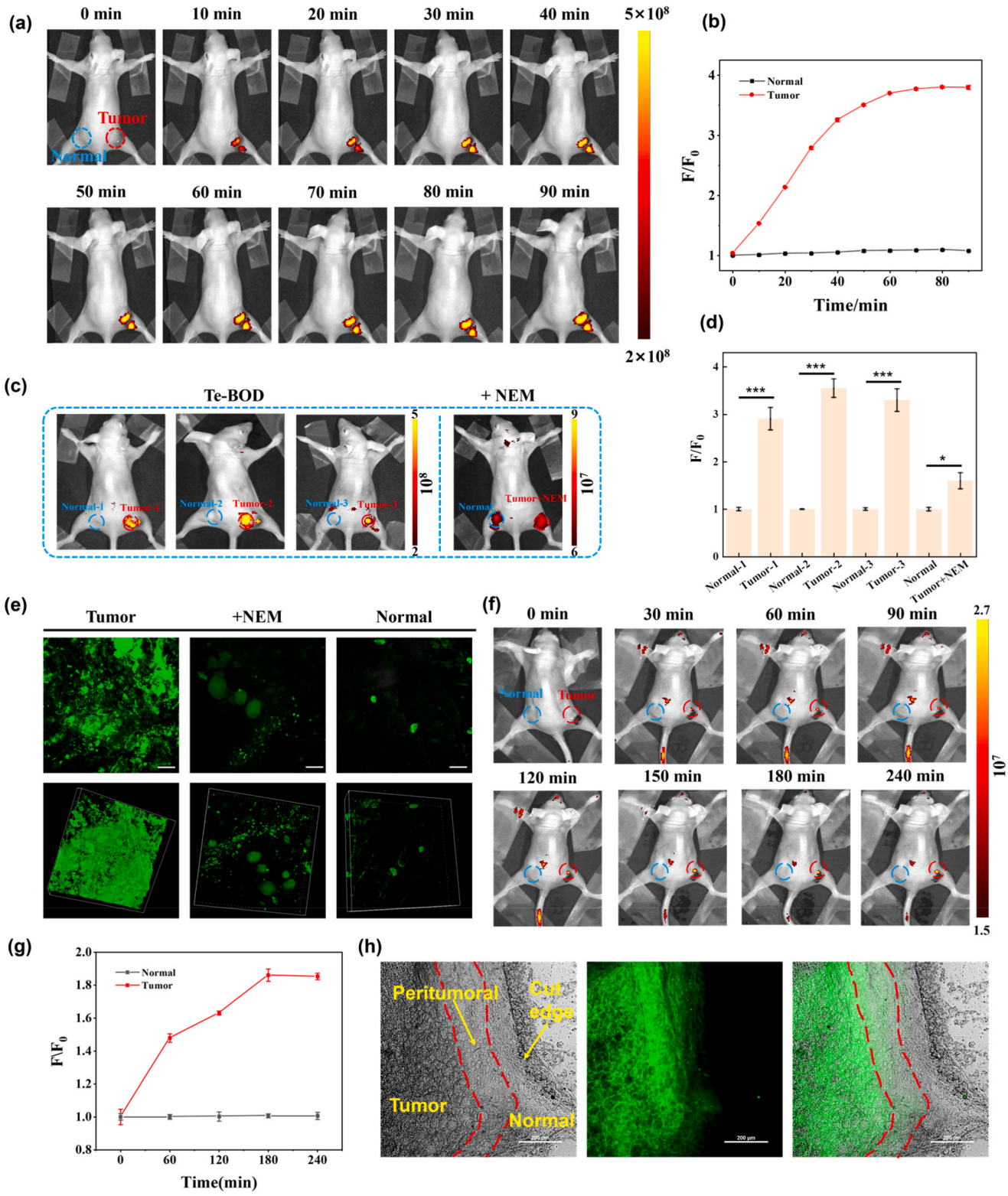

Fig. 4. In vivo fluorescent imaging of endogenous GSH in the LA795-tumor-bearing mice with **Te-BOD** (200 μM, 25 μL in PBS/DMSO, v/v = 5:5, pH 7.4). (a) Real-time imaging of tumor and normal tissue in intratumoral injected tumor-bearing mice. (b) Time-dependent F/F_0 (Normal or Tumor/Blank) of normal and tumor area as shown in (a). (c) Fluorescence imaging of tumor and normal tissue in different tumor-bearing mice 70 min after probe injection and pretreated with 5 mM NEM for 30 min then intratumoral injection of the probe. (d) Relative fluorescence intensity in (c) (*P < 0.1, **P < 0.01, ***P < 0.001, ****P < 0.0001). (e) Confocal imaging of tumor tissue, tumor + 5 mM NEM and normal tissue samples that were soaked in the probe solution for 30 min λ_{ex} = 490 nm, λ_{em} = 510–550 nm. Scale bar: 100 μm. (f) Time-dependent fluorescence imaging of intravenous probes. (g) Relative fluorescence intensity in (f). (h) The tumor was excised 180 min following intravenous probe injection. The tumor tissue along with a small quantity of adjacent normal tissue was removed simultaneously, and confocal imaging was conducted. λ_{ex} = 490 nm, λ_{em} = 510–550 nm. Scale bar: 200 μm.

tumor tissue exhibited intense fluorescence due to the high GSH content, whereas the NEM group and normal tissue displayed weak fluorescence due to the low GSH content, which was in accordance with the outcomes of in vivo imaging. H&E staining was applied to the normal tissue and subcutaneous tumor tissue of mice, as shown in Fig. S18. The cells in the normal tissue were arranged orderly with a clear tissue structure, while the tumor tissue appeared dark and unevenly arranged. Many dark blue spots were observed, which might be attributed to apoptosis and necrosis in the tumor tissue. This result was consistent with the detection result of the Te-BOD, thereby verifying the accuracy of the probe for tumor detection. Benefitting from the high-threshold response, the probe will not be activated by GSH in the blood during circulation, as the GSH content in blood of tumor-bearing mouse is approximately in the range of 200–300 μM [54]. Thus, we also employ intravenous probe to study the ability of discrimination tumors from normal tissues (Fig. 4f). Following intravenous injection of the probe, the fluorescence at the tumor site gradually intensified with the passage of time, whereas there was scarcely any notable fluorescence alteration in normal tissue. Three hours after the intravenous probe, the fluorescence of the tumor site reached its plateau, demonstrating approximately 1.8 times the fluorescence enhancement compared to normal tissue, effectively achieving the discrimination between tumor and normal tissue (Fig. 4g). Our objective is not merely to discriminate between tumor and normal tissue via the probe, but also to observe the boundary between them, as this

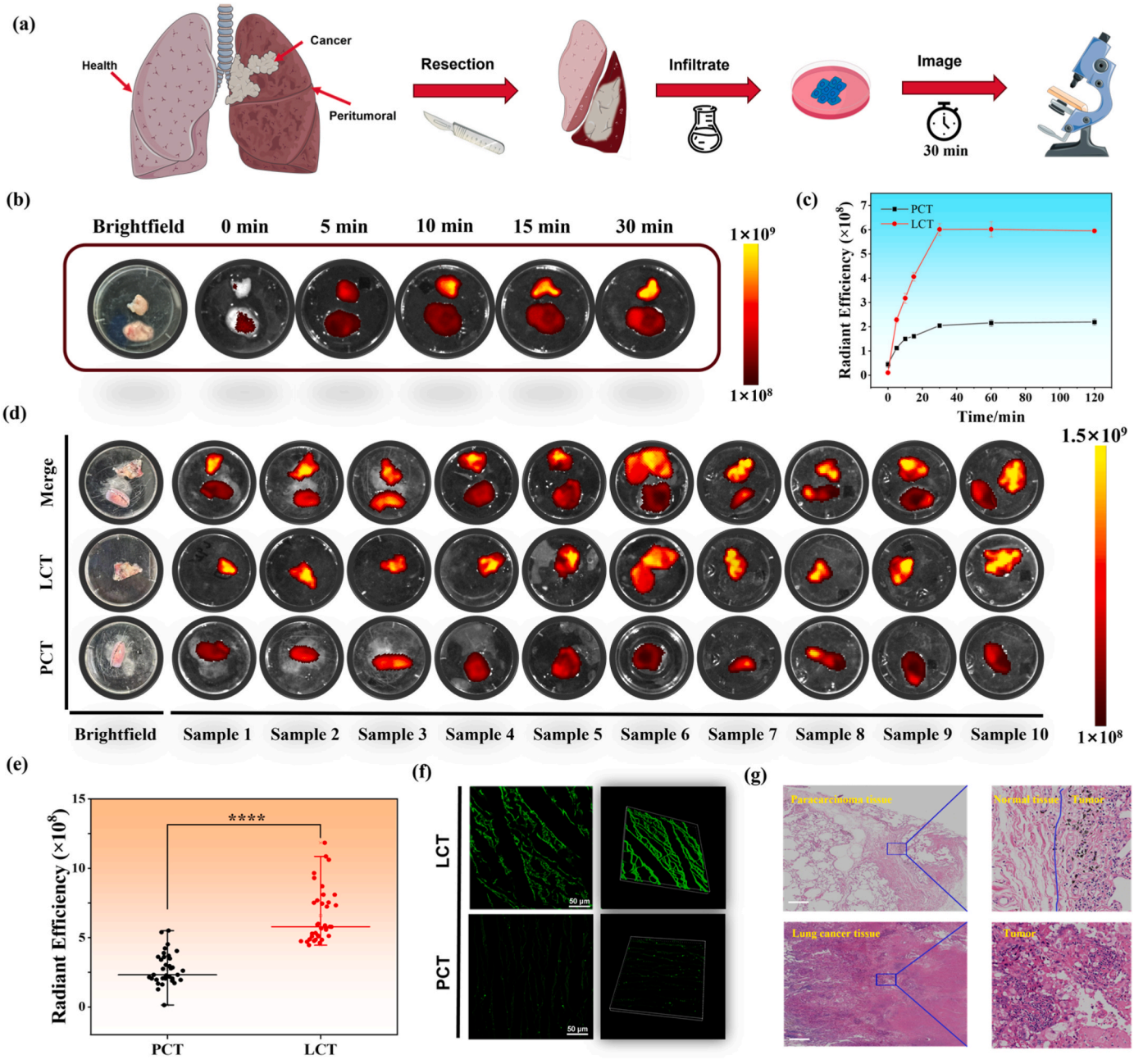

Fig. 5. Fluorescence imaging of lung cancer and para-cancer tissues. (a) Schematic illustration of a **Te-BOD** employed for fluorescence imaging of lung cancer and para-cancer tissues. (b) Time-dependent of fluorescence imaging in probe-soaked lung cancer tissue and adjacent tissue. (c) Relative fluorescence intensity in (b). (d) Fluorescence imaging of clinical lung cancer tissue (LCT) and para-cancer tissue (PCT) samples that were soaked in the probe solution for 30 min. (e) Relative fluorescence intensity in (d). (f) Confocal imaging of clinical lung cancer tissue and para-cancer tissue samples that were soaked in the probe solution for 30 min λ_{ex} = 490 nm, λ_{em} = 510–550 nm. Scale bar: 50 μm (g) Representative H&E-stained sections of the clinical lung cancer tissue and para-cancer tissue samples. Scale bar: 500 μm *P < 0.1, **P < 0.01, ***P < 0.001, ****P < 0.0001.

will enable the removal of the least amount of normal tissue possible during surgery. The tumor and a small amount of adjacent tissue were removed and confocal imaging was performed 3 h after intravenous injection into the tumor-bearing mice. As shown in Fig. 4h, we can distinctly observe the alteration of fluorescence intensity from cancerous tissue to normal tissue. The cancer tissue exhibited intense fluorescence, the adjacent tissue displayed relatively weak fluorescence, and the normal tissue manifested almost no fluorescence. Finally, we established a metastatic pneumonia disease model using B16 cells and conducted fluorescence imaging by spraying a probe. As depicted in Fig. S19, the lungs with inflammation exhibited local fluorescence enhancement (approximately 2–2.5 times compared to normal tissues); however, the obvious lesions were difficult to observe with the naked eye, which demonstrated that the probe was capable of detecting the inflammation site through fluorescence imaging. These experimental results manifest that the probe can reliably distinguish between cancerous and normal tissues based on the disparity in GSH content.

3.5. *Imaging clinical lung cancer and para-cancer tissue by Te-BOD*

Inspired by the outstanding performance of **Te-BOD** in discriminating orthotopic tumors from normal tissue in mice, we further utilized the probe to distinguish fresh human lung cancer tissues from para-cancerous tissues derived from clinical surgical samples (Fig. 5a). Firstly, lung cancer tissue and para-cancer tissue were soaked in the probe solution to monitor the fluorescence trend of the two tissues over time. As time elapsed, the fluorescence in both tissues gradually intensified and reached saturation at 30 min (Fig. 5b). The real-time confocal imaging at the tissue level is also consistent with this conclusion (Fig. S20). The fluorescence in lung cancer tissue was about 3-fold than that in adjacent tissue, thereby enabling reliable discrimination of cancerous tissue (Fig. 5c). Subsequently, more clinical samples were imaged (Fig. 5d). It was noted that all the phenomenon was consistent, and the fluorescence intensity of lung cancer tissues was higher than that of para-cancer tissues, with a statistically significant difference (Fig. 5e). Furthermore, the fluorescence imaging of the probe-soaked lung tissue slices under confocal microscopy also indicated that the fluorescence of lung cancer tissue was more intense (Fig. 5f). We further validated the accuracy of the detection results through H&E staining (Fig. S21). As depicted in Fig. 5g, the lung cancer tissue exhibited a greater number of black spots, suggesting severe inflammation and lesions within the cancerous tissue. Meanwhile, the adjacent cancerous tissue presented partial lesions, and the boundary of the tissue gradually transitioning from cancerous to normal could be observed. This outcome further substantiated the accuracy of our probe in discriminating between cancerous and para-cancer tissues. Histological examination is mainly applied to tumor tissue, and H&E staining serves as the gold standard for this examination as it enables the observation and analysis of the tissue structure and has the merits of low cost. Nevertheless, H&E staining has certain limitations, such as the poor staining of some tissue structures and the inability to display intracellular details. Additionally, this method is complex and time-consuming, often requiring at least three days to obtain results. In contrast to H&E staining, our probe is more accessible to enter cells, can differentiate normal tissue from tumor by fluorescence intensity, featuring a fast response and simple operation, and possesses better clinical diagnostic value. Most importantly, it exhibits capability in delineating tumor margins with remarkable precision.

4. Conclusion

We developed a novel probe with an elevated biomarker response-threshold and ER-targeting ability for successfully enhancing clinical precision in lung cancer tissue discrimination. Owing to the steric hindrance effect, the PTE recognition groups significantly raise the response-threshold to GSH, nearly a hundred-fold improvement over previous GSH probes. Meanwhile, the probe possesses strong lipid solubility, which is beneficial for the rapid targeting of ER. This design strategy enhances the response-threshold of the probe, and ingeniously positions the response range of the probe to GSH within the endogenous GSH content in ER. Owing to the outstanding sensing performance of the probe, we successfully accomplished the precise discrimination between normal cells and cancer cells, and further manifested the capacity of the probe to distinguish the two types of cells via normal cells and cancer cells mixed culture fluorescence imaging experiments. The probe demonstrated approximately 4-fold fluorescence enhancement in the tumor compared to normal tissues. Furthermore, using this probe, a distinct bright fluorescence signal from tumors could be observed in confocal imaging of tumor tissues from tumor-bearing mice after intravenous injection, in stark contrast to the limited fluorescence emanating from normal tissues. Finally, we also discriminated clinical lung cancer tissue from para-cancer tissue using the probe and verified our results through the gold standard H&E staining. These results demonstrated that **Te-BOD** can serve as a crucial research tool and holds potential applications in cancer diagnosis and clinical application of intraoperative assisted resection in the future.

CRediT authorship contribution statement

Zhiyang Yuwen: Writing – original draft, Methodology, Investigation, Formal analysis, Data curation, Conceptualization. **Xinglong Chen:** Software, Resources. **Kexin Chen:** Visualization. **Tenglong Zou:** Validation, Software, Formal analysis. **Guojiang Mao:** Writing – review & editing. **Hongwen Liu:** Writing – review & editing, Supervision, Project administration, Conceptualization. **Lemeng Zhang:** Writing – review & editing, Supervision, Project administration, Funding acquisition.

Declaration of competing interest

The authors declare that they have no known competing financial interests or personal relationships that could have appeared to influence the work reported in this paper.

Acknowledgments

This work was supported by the National Natural Science Foundation of China (Grants 22474036) and supported by grants from the National Natural Science Foundation of Hunan Province (2023JJ60039, 2023JJ40412), the Open Research Fund of the School of Chemistry and Chemical Engineering, Henan Normal University (2024Y04).

Appendix A. Supplementary data

Supplementary data to this article can be found online at https://doi.org/10.1016/j.mtbio.2025.101654.

Data availability

Data will be made available on request.

References

[1] S.J. Henley, E.M. Ward, S. Scott, J. Ma, R.N. Anderson, A.U. Firth, C.C. Thomas, F. Islami, H.K. Weir, D.R. Lewis, R.L. Sherman, M. Wu, V.B. Benard, L. C. Richardson, A. Jemal, K. Cronin, B.A. Kohler, Annual report to the nation on the status of cancer, part I: National cancer statistics, Cancer 126 (2020) 2225–2249.
[2] X. Zhang, F. Yu, Z. Wang, T. Jiang, X. Song, F. Yu, Fluorescence probes for lung carcinoma diagnosis and clinical application, Sens. Diagn 2 (2023) 1077–1096.
[3] T. Yoshikawa, N. Ishiwa, S. Morinaga, Y. Noguchi, Y. Yamamoto, Can surgical diagnosis of "early" gastric cancer and lymph node metastasis be accurate? Gastric Cancer 7 (2004) 36–40.
[4] S. Blair, M. Garcia, T. Davis, Z. Zhu, Z. Liang, C. Konopka, K. Kauffman, R. Colanceski, I. Ferati, B. Kondov, S. Stojanoski, M.B. Todorovska, N.

T. Dimitrovska, N. Jakupi, D. Miladinova, G. Petrusevska, G. Kondov, W. L. Dobrucki, S. Nie, V. Gruev, Hexachromatic bioinspired camera for image-guided cancer surgery, Sci. Transl. Med. 13 (2021) eaaw7067.
[5] K. Wang, C. Liu, H. Zhu, Y. Zhang, M. Su, X. Wang, M. Liu, X. Rong, B. Zhu, Recent advances in small-molecule fluorescent probes for diagnosis of cancer cells/tissues, Coord. Chem. Rev. 477 (2023) 214946.
[6] R.W. Gao, N.T. Teraphongphom, N.S. van den Berg, B.A. Martin, N.J. Oberhelman, V. Divi, M.J. Kaplan, S.S. Hong, G. Lu, R. Ertsey, W.S.F.J. Tummers, A.J. Gomez, F. C. Holsinger, C.S. Kong, A.D. Colevas, J.M. Warram, E.L. Rosenthal, Determination of tumor margins with surgical specimen mapping using near-infrared fluorescence, Cancer Res. 78 (2018) 5144–5154.
[7] L.J. Lauwerends, P.B.A.A. van Driel, R.J. Baatenburg de Jong, J.A.U. Hardillo, S. Koljenovic, G. Puppels, L. Mezzanotte, C.W.G.M. Löwik, E.L. Rosenthal, A. L. Vahrmeijer, S. Keereweer, Real-time fluorescence imaging in intraoperative decision making for cancer surgery, Lancet Oncol. 22 (2021) e186–e195.
[8] Q.-J. Duan, Z.-Y. Zhao, Y.-J. Zhang, L. Fu, Y.-Y. Yuan, J.-Z. Du, J. Wang, Activatable fluorescent probes for real-time imaging-guided tumor therapy, Adv. Drug Deliv. Rev. 196 (2023) 114793.
[9] R.K. Orosco, R.Y. Tsien, Q.T. Nguyen, Fluorescence imaging in surgery, IEEE Reviews in Biomedical Engineering 6 (2013) 178–187.
[10] Y. Lv, M. Liu, Y. Zhang, X. Wang, F. Zhang, F. Li, W.-E. Bao, J. Wang, Y. Zhang, W. Wei, G. Ma, L. Zhao, Z. Tian, Cancer cell membrane-biomimetic nanoprobes with two-photon excitation and near-infrared emission for intravital tumor fluorescence imaging, ACS Nano 12 (2018) 1350–1358.
[11] H.-W. Liu, L. Chen, C. Xu, Z. Li, H. Zhang, X.-B. Zhang, W. Tan, Recent progresses in small-molecule enzymatic fluorescent probes for cancer imaging, Chem. Soc. Rev. 47 (2018) 7140–7180.
[12] D. Wu, A.C. Sedgwick, T. Gunnlaugsson, E.U. Akkaya, J. Yoon, T.D. James, Fluorescent chemosensors: the past, present and future, Chem. Soc. Rev. 46 (2017) 7105–7123.
[13] H. Li, Q. Yao, W. Sun, K. Shao, Y. Lu, J. Chung, D. Kim, J. Fan, S. Long, J. Du, Y. Li, J. Wang, J. Yoon, X. Peng, Aminopeptidase N activatable fluorescent probe for tracking metastatic cancer and image-guided surgery via in situ spraying, J. Am. Chem. Soc. 142 (2020) 6381–6389.
[14] Y. Chen, T. Xiong, J. Du, J. Fan, X. Peng, Tumor-specific cascade recognition of activatable probes for fluorescence navigation surgery, CCS Chem. 0 (2024) 1–12.
[15] S. Chen, F. Chen, Y. Li, Y. Wang, X. Wang, C. Ye, A fluorescein derivative chemosensor combined with triplet–triplet annihilation upconversion system for ratiometric sensing of cysteine, J. Anal. Test. 7 (2023) 369–376.
[16] Y. Wang, Y. Hu, D. Ye, Activatable multimodal probes for in vivo imaging and theranostics, Angew. Chem. Int. Ed. 61 (2022) e202209512.
[17] Y. Zhang, G. Zhang, Z. Zeng, K. Pu, Activatable molecular probes for fluorescence-guided surgery, endoscopy and tissue biopsy, Chem. Soc. Rev. 51 (2022) 566–593.
[18] H. Li, D. Kim, Q. Yao, H. Ge, J. Chung, J. Fan, J. Wang, X. Peng, J. Yoon, Activity-based NIR enzyme fluorescent probes for the diagnosis of tumors and image-guided surgery, Angew. Chem. Int. Ed. 60 (2021) 17268–17289.
[19] J. Liu, M. Liu, H. Zhang, W. Guo, High-contrast fluorescence diagnosis of cancer cells/tissues based on β-lapachone-triggered ROS amplification specific in cancer cells, Angew. Chem. Int. Ed. 60 (2021) 12992–12998.
[20] Y. Shen, W. Li, Z. Zhou, J. Xu, Y. Li, H. Li, X. Zheng, S. Liu, X.-B. Zhang, L. Yuan, Dual-locked fluorescent probes activated by aminopeptidase N and the tumor redox environment for high-precision imaging of tumor boundaries, Angew. Chem. Int. Ed. 63 (2024) e202406332.
[21] F. Wang, Y. Zhu, L. Zhou, L. Pan, Z. Cui, Q. Fei, S. Luo, D. Pan, Q. Huang, R. Wang, C. Zhao, H. Tian, C. Fan, Fluorescent in situ targeting probes for rapid imaging of ovarian-cancer-specific γ-glutamyltranspeptidase, Angew. Chem. Int. Ed. 54 (2015) 7349–7353.
[22] X. Li, P. Wu, W. Cao, H. Xiong, Development of pH-activatable fluorescent probes for rapid visualization of metastatic tumours and fluorescence-guided surgery via topical spraying, Chem. Commun. 57 (2021) 10636–10639.
[23] F. Yu, Y. Wang, C. Yu, W. Zhang, X. Bai, Sensitive and specific Y-shaped ratio biosensor for detecting serum miR-18a: potential early scanning tool for non-small cell lung cancer, J. Anal. Test. 8 (2024) 237–244.
[24] H. Jeong, X. Wu, J.-S. Lee, J. Yoon, Recent advances in enzyme-activated NIR fluorescent probes for biological applications, TrAC, Trends Anal. Chem. 168 (2023) 117335.
[25] L. Wu, J. Huang, K. Pu, T.D. James, Dual-locked spectroscopic probes for sensing and therapy, Nat. Rev. Chem 5 (2021) 406–421.
[26] J.M. Estrela, A. Ortega, E. Obrador, Glutathione in cancer biology and therapy, Crit. Rev. Clin. Lab Sci. 43 (2006) 143–181.
[27] H. Fan, G. Yan, Z. Zhao, X. Hu, W. Zhang, H. Liu, X. Fu, T. Fu, X.-B. Zhang, W. Tan, A smart photosensitizer–manganese dioxide nanosystem for enhanced photodynamic therapy by reducing glutathione levels in cancer cells, Angew. Chem. Int. Ed. 55 (2016) 5477–5482.
[28] S. Lee, J. Li, X. Zhou, J. Yin, J. Yoon, Recent progress on the development of glutathione (GSH) selective fluorescent and colorimetric probes, Coord. Chem. Rev. 366 (2018) 29–68.
[29] Z. Liu, X. Zhou, Y. Miao, Y. Hu, N. Kwon, X. Wu, J. Yoon, A reversible fluorescent probe for real-time quantitative monitoring of cellular glutathione, Angew. Chem. Int. Ed. 56 (2017) 5812–5816.
[30] Q. Zeng, Z. Yuwen, L. Zhang, Y. Li, H. Liu, K. Zhang, Molecular engineering of a doubly quenched fluorescent probe enables ultrasensitive detection of biothiols in highly diluted plasma and high-fidelity imaging of dihydroartemisinin-induced ferroptosis, Anal. Chem. 96 (2024) 13260–13269.
[31] J. Qin, H. Tian, F. Kong, Y. Guo, W. Du, C. Zhang, H. Gu, Y. Li, Construction of GSH activated near-infrared fluorescent and photoacoustic dual-modal probe for in vivo tumor imaging, Sensor. Actuat. B-Chem. 371 (2022) 132522.
[32] M.Y. Lucero, J. Chan, Photoacoustic imaging of elevated glutathione in models of lung cancer for companion diagnostic applications, Nat. Chem. 13 (2021) 1248–1256.
[33] D. Cheng, J. Peng, Y. Lv, D. Su, D. Liu, M. Chen, L. Yuan, X. Zhang, De novo design of chemical stability near-infrared molecular probes for high-fidelity hepatotoxicity evaluation in vivo, J. Am. Chem. Soc. 141 (2019) 6352–6361.
[34] L.-L. Wang, Q. Xu, Y.-Z. Xie, Y.-R. Zhang, M.-H. Zheng, X.-F. Li, J.-Y. Jin, A triple-targeting fluorescent probe reveals the glutathione and viscosity crosstalk in mitochondria, endoplasmic reticulum, and nucleoli in cells during ferroptosis, Sensor. Actuat. B-Chem. 399 (2024) 134872.
[35] C.-S. Jiang, Z.-Q. Cheng, Y.-X. Ge, J.-L. Song, J. Zhang, H. Zhang, An endoplasmic reticulum-targeting fluorescent probe for the imaging of GSH in living cells, Anal. Methods 11 (2019) 3736–3740.
[36] X. Song, X. Wang, Y. Wang, Y. Hao, C. Li, L. Chai, H. Ren, J. Chen, W. Hu, T. D. James, Monitoring glutathione content of the endoplasmic reticulum under scrap leather-induced endoplasmic reticulum stress via an endoplasmic reticulum-targeted two-photon fluorescent probe, Anal. Chem. 96 (2024) 18132–18140.
[37] L.-L. Wang, Y.-R. Zhang, M.-H. Zheng, X. Wang, X. Wu, J.-Y. Jin, A single fluorescent probe reveals changes in endoplasmic reticulum–mitochondria contact in hepatocytes during ferroptosis, Chem. Eng. J. 466 (2023) 143104.
[38] Y. Zhao, L. Li, Q. Ye, Y. Gong, R. Yang, H. Liu, Reaction-activated disassembly of the NIR-II probe enables fast detection and ratiometric photoacoustic imaging of glutathione in vivo, Anal. Chem. 95 (2023) 14043–14051.
[39] Z. Yuwen, T. Zou, Z. He, Z. Su, Y. Gong, H. Liu, R. Yang, FRET-based nanoprobe with adaptive background suppression for reliable detection of $ONOO^-/ClO^-$ in whole blood: facilitating monitoring of sepsis progression and hemolytic disorders, Anal. Chem. (2024) 20318–20329.
[40] R.W. Sabnis, T.G. Deligeorgiev, M.N. Jachak, T.S. Dalvi, DiOC6(3): a useful dye for staining the endoplasmic reticulum, Biotech. Histochem. 72 (1997) 253–258.
[41] Q. Tang, H. Li, H. Hu, L. Chen, New tool for diseases mechanism studies: endoplasmic reticulum-targeted fluorescent probes, Dyes Pigments 219 (2023) 111634.
[42] H. Ma, Y. Lu, Z. Huang, S. Long, J. Cao, Z. Zhang, X. Zhou, C. Shi, W. Sun, J. Du, J. Fan, X. Peng, ER-targeting cyanine dye as an NIR photoinducer to efficiently trigger photoimmunogenic cancer cell death, J. Am. Chem. Soc. 144 (2022) 3477–3486.
[43] A. Fujisawa, T. Tamura, Y. Yasueda, K. Kuwata, I. Hamachi, Chemical profiling of the endoplasmic reticulum proteome using designer labeling reagents, J. Am. Chem. Soc. 140 (2018) 17060–17070.
[44] D. Singh, D. Rajput, S. Kanvah, Fluorescent probes for targeting endoplasmic reticulum: design strategies and their applications, Chem. Commun. 58 (2022) 2413–2429.
[45] J. Yin, L. Huang, L. Wu, J. Li, T.D. James, W. Lin, Small molecule based fluorescent chemosensors for imaging the microenvironment within specific cellular regions, Chem. Soc. Rev. 50 (2021) 12098–12150.
[46] N. Li, T. Wang, N. Wang, M. Fan, X. Cui, A substituted-rhodamine-based reversible fluorescent probe for in vivo quantification of glutathione, Angew. Chem. Int. Ed. 62 (2023) e202217326.
[47] Y. Zhang, J. Zhang, M. Su, C. Li, Rational molecular design of a reversible BODIPY-Based fluorescent probe for real-time imaging of GSH dynamics in living cells, Biosens. Bioelectron. 175 (2021) 112866.
[48] J. Chen, H. Liu, W. Xie, M. Gu, G. Mao, S. Yang, Recent progress in endoplasmic reticulum-targetable small-molecule probes for fluorescence sensing and phototherapy, J. Anal. Test. 7 (2023) 304–324.
[49] Y. Koide, M. Kawaguchi, Y. Urano, K. Hanaoka, T. Komatsu, M. Abo, T. Terai, T. Nagano, A reversible near-infrared fluorescence probe for reactive oxygen species based on Te–rhodamine, Chem. Commun. 48 (2012) 3091–3093.
[50] S.M. Kondengadan, B. Wang, Quantitative factors introduced in the feasibility analysis of reactive oxygen species (ROS)-Sensitive triggers, Angew. Chem. Int. Ed. 63 (2024) e202403880.
[51] H. Wang, X. Zhang, M. Dong, W. Zhang, W. Zhang, P. Li, B. Tang, Evaluation of effectiveness of antiarthritic treatment by in situ ratiometric fluorescence imaging of the endoplasmic reticulum pH, Sensor. Actuat. B-Chem. 349 (2021) 130786.
[52] D. Montero, C. Tachibana, J. Rahr Winther, C. Appenzeller-Herzog, Intracellular glutathione pools are heterogeneously concentrated, Redox Biol. 1 (2013) 508–513.
[53] H. Lv, C. Zhen, J. Liu, P. Yang, L. Hu, P. Shang, Unraveling the potential role of glutathione in multiple forms of cell death in cancer therapy, Oxid. Med. Cell. Longev. 2019 (2019) 3150145.
[54] V.r. Serru, B. Baudin, F.d.r. Ziegler, J.-P. David, M.-J.p. Cals, M. Vaubourdolle, N. Mario, Quantification of reduced and oxidized glutathione in whole blood samples by capillary electrophoresis, Clin. Chem. 47 (2001) 1321–1324.